Electronic Supplementary Material (ESI) for Journal of Materials Chemistry A.

Electronic Supplementary Information

Electrolyte ions-matching hierarchically porous biochar electrodes with an extended potential window for next-generation supercapacitors

Ganji Seeta Rama Raju[1], *Svyatoslav Kondrat*[2,3], *Nilesh R. Chodankar*[4], *Seung-Kyu Hwang*[5], *Jeong Han Lee*[6], *Teng Long*[7], *Eluri Pavitra*[5], *Swati J. Patil*[1], *Kugalur Shanmugam Ranjith*[1], *M. V. Basaveswara Rao*[8], *Peng Wu*[9,*], *Kwang Chul Roh*[6,*], *Yun Suk Huh*[5,*], *and Young-Kyu Han*[1,*]

[1]Department of Energy and Materials Engineering, Dongguk University-Seoul, Seoul 04620, Republic of Korea.

[2]Institute of Physical Chemistry, Polish Academy of Sciences, Warsaw, Poland

[3]Institute for Computational Physics, University of Stuttgart, Stuttgart, Germany

[4]Mechanical Engineering Department, Khalifa University, Abu Dhabi 127788, United Arab Emirates

[5]Department of Biological Engineering, Biohybrid Systems Research Center (BSRC), Inha University, Incheon, 22212, Republic of Korea.

[6]Energy & Environmental Division, Korea Institute of Ceramic Engineering & Technology, 101, Soho-ro, Jinju-si, Gyeongsangnam-do 660-031, Republic of Korea.

[7]Department of Energy and Power Engineering, Huazhong University of Science and Technology, Wuhan 430074, China.

[8]Dapartment of Chemistry, Krishna University, Machilipatnam, Andhra Pradesh-521001, India

[9]College of Energy and Power Engineering, and Ministry of Education, Inner Mongolia University of Technology, Hohhot, 010051, China

Characterizations: The SGC and SHAC samples morphological properties were examined with HRSEM (Hitachi-SU8010, Japan) system and FETEM (JEOL, JEM 2100F, Japan) equipment. Platinum coating was sprayed on the sample surfaces by using Quorum technology ion sputter coater (Q-150T, United Kingdom) to avoid possible charging of specimens before FESEM observation was made. The EDS and elemental mappings were obtained from the EDX spectroscopy measurements, which were equipped with FETEM system. The phase purity of SHAC samples were characterized by XRD (X-pert Powder Diffractometer, Pro MRD, PANalytical, The Netherlands) analysis. The XPS (K-Alpha, Thermo Scientific, USA) and Raman spectra (WITEC alpha 300R, Germany) were measured to identify the surface chemical composition, oxidation states and surface functional groups. The N_2 adsorption/desorption isotherms of the SHAC and CAC samples were measured with a BET surface analyzer (Tristar, ASAP 2020, Micromeritics, USA).

Electrochemical Equations:

$$C_{sp}\ (\mathrm{F/g})\ \text{with GCD} = \frac{I \times \Delta t}{m \times \Delta V} \quad \text{(or)} \quad C_v\ (F/cm^3) = \rho \times C_{sp} \quad \text{(or)}$$

$$C_{sp}(\mathrm{F/g})\ \text{with CV} = \frac{Integral\ area\ under\ CV\ curve}{2\ X\ Scan\ rate\ X\ \Delta V\ X\ m} \qquad \text{(S1)}$$

$$E_{d(specific)}\ (\mathrm{Wh/kg}) = \frac{C_{sp} \times \Delta V^2}{7.2} \quad \text{(or)} \quad E_{d(volumetric)}\ (Wh/cm^3) = \frac{C_v \times \Delta V^2}{7.2} \qquad \text{(S2)}$$

$$P_d\ (\mathrm{W/kg}) = \frac{E_{d(specific)}}{\Delta t} \times 3600 \quad \text{(or)}\ P_d\ (\mathrm{W/cm^3}) = \frac{E_{d(volumetric)}}{\Delta t} \times 3600 \qquad \text{(S3)}$$

where C_{sp}, C_v, E_d, and P_d represents the specific capacitance, volumetric capacitance, energy density and power density, respectively. I is the applied current, Δt is the discharge time, m is the mass of active material on the electrode, ΔV is the potential window and ρ is the density of active material i.e., 0.5 kg/L.

Note: The density of the active material was analyzed by tamping procedure with the formula

Density= mass/volume

The SHAC2 sample was poured into a 10 ml graduated cylinder and the cylinder was tapped gently until no air bubbles remained. The volume of the sample was read as 2 ml from the cylinder scale. The mass of the sample was calculated by subtracting the mass of the empty cylinder from the mass of the cylinder with the sample.

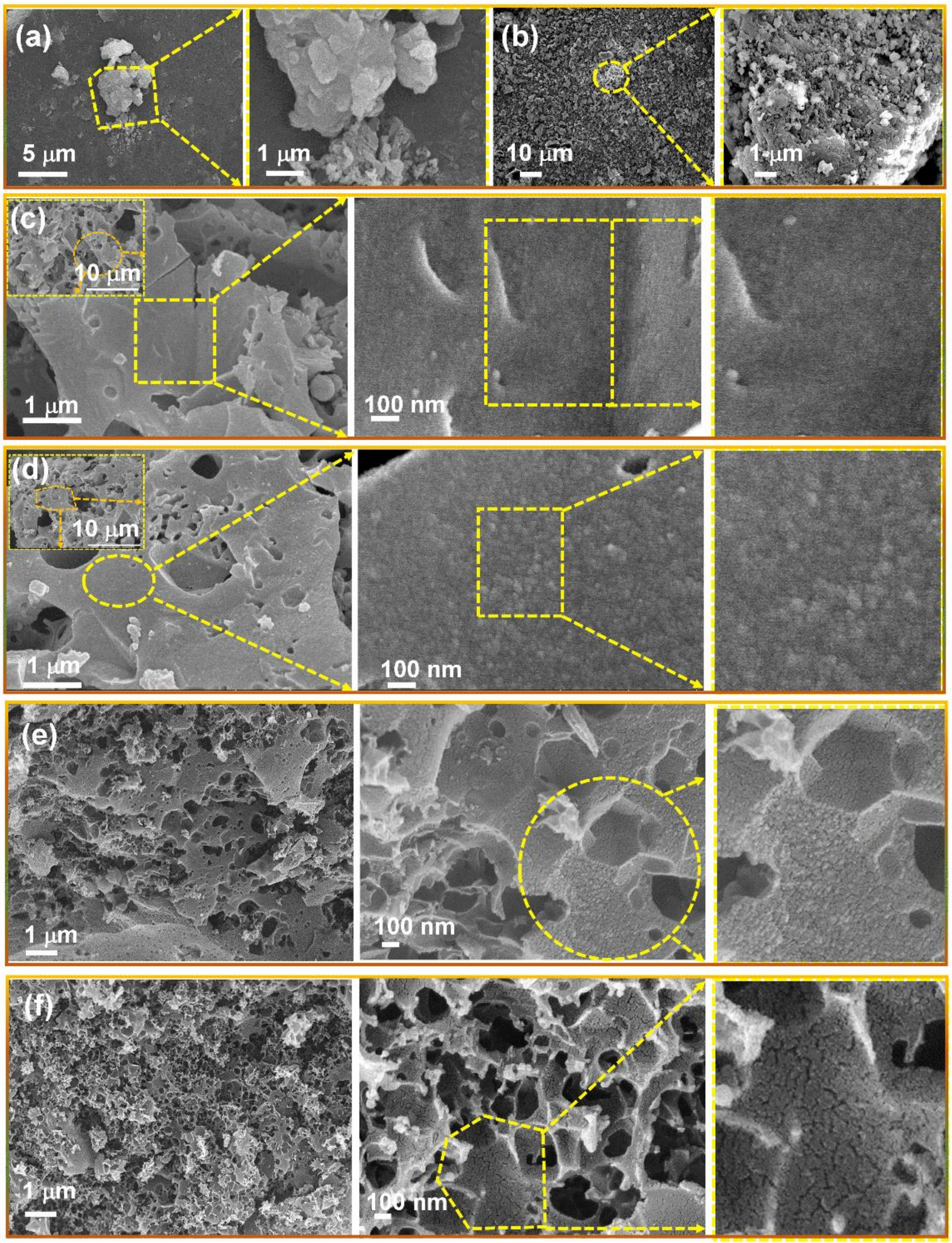

Fig. S1 Morphological and elemental analyses: FESEM images of the (a) milled raw SG particles after removing the non-lignocellulosic components, (b) after carbonization at 600 °C, (c) SHAC0.5, (d) SHAC1, (e) SHAC3, and (e) SHAC4.

Energy Dispersive X-ray analysis: The EDXA (Fig. S2a) from the FETEM analysis authorizes the presence only of carbon (C) and oxygen (O) without any other functional groups. Additionally, EDXA spectra show that both C and O occupy K shells at 0.277 and 0.525 keV, respectively.

Note 1

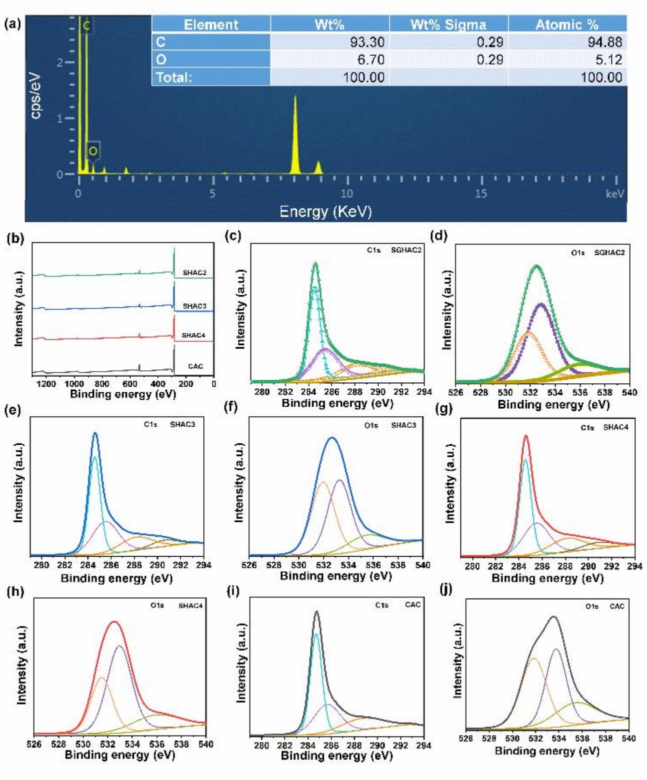

Element	Wt%	Wt% Sigma	Atomic %
C	93.30	0.29	94.88
O	6.70	0.29	5.12
Total:	100.00		100.00

Fig. S2 (a) EDS spectrum confirms the presence of C and O and the related atomic and weight percentages are presented in the inset. ***XPS analysis***: (b) survey scans of SHAC samples, and high-resolution XPS spectra of (c & d) C1s and O1s of SHAC2; (e&f) C1s and O1s SHAC3; (g&h) C1s and O1s SHAC4; (i &j) C1s and O1s of CAC.

The surface chemistry of the SHAC and commercially available AC (CAC, MTI, Korea) samples were investigated via XPS. All the samples displayed similar compositions (Fig. S2b). The XPS survey scans of all SHAC samples (Fig. S2b) exhibit C1s (285.6 eV) and O1s (531.7 eV) peaks without considerable traces of other elements. This indicates the successful removal of chemical residues from activation after several cycles of washing. Fig. S2c and Fig. S2d shows the high-resolution (HR)-XPS spectra of C1s and O1s of SHAC2. Fig. S2e &f, Fig. S2g & h and Fig. S2i &j show HR-XPS spectra of C1s and O1s of SHAC3 and SHAC4. As shown in Fig. S2c, the HR C1s spectrum of SHAC2 deconvolutes into four peaks that are attributed to sp^2 hybridised carbon: C–C (284.5 eV), C–O (285.5 eV), O–C=O (288.4 eV), and the shake-up satellite peak at 290.8 eV.[S1-S2] The peak at 284.5 eV confirms the amorphous nature of the SHAC, which is congruent with XRD pattern [S3]. Likewise, the HR O1s spectrum of SHAC2 deconvolutes into three components (Fig. S2d): 531.6 (C=O), 532.8 (C–O), and 536.1 (O–C=O) eV. These are related to K_2CO_3, $KHCO_3$, and KOH.[S2, S4-S5] The C1s and O1s oxygen functional groups are in good agreement with each other. The XPS exhibits atomic percentage ratios (C/O) for SHAC2, SHAC3, and SHAC4 of 13.99, 18.75, and 12.98, respectively. These are in good agreement with the EDS analysis.

Chemical reactions during activation process:

$$6\mathrm{KOH} + 2\mathrm{C} \xrightarrow{400℃} 2\mathrm{K} + 3\mathrm{H_2} + 2\mathrm{K_2CO_3} \quad \text{(SR1)}$$

$$\mathrm{K_2CO_3} \xrightarrow{600℃} \mathrm{K_2O} + \mathrm{CO_2} \quad \text{(SR2)}$$

$$\mathrm{K_2CO_3} + 2\mathrm{C} \xrightarrow{900℃} 2\mathrm{K} + 3\mathrm{CO} \quad \text{(SR3)}$$

Note 2

To study the electrolyte dependent electrochemical kinetics of SHAC2 electrodes, the electrochemical impedance spectroscopy (EIS) measurements were carried out at an open circuit potential between 0.1 Hz and 100 kHz with an alternating current (ac) amplitude of 5 mV, and the obtained results are presented in Fig. S3. It is familiar that the width of the semicircle in the real part exemplifies the charge transfer resistance (R_{ct}) and the vertical or slanted line along –Z" direction in the low frequency region related to the diffusion control process. Evidently, the Nyquist plots of EIS in Fig. S3 exhibited the quasi-semicircles with nearly vertical lines in the high and low frequency regions, respectively, demonstrating the capacitive behaviour of SHAC2 electrode. The Nyquist plots exhibited the Rct values of about 0.15, 0.41 and 0.44 Ω when measured in the KOH, Na_2SO_4, and H_2SO_4 electrolytes, respectively. Also, when EIS of SHAC2 electrode measured in the KOH electrolyte, vertical line exhibited almost perpendicular to the Z' direction as compared to the EIS measurements in Na_2SO_4 and K_2SO_4 electrolytes where vertical line slanted slightly, indicating the fast ion diffusion pathways in the KOH electrolyte during electrochemical operation with dominant capacitive behaviour of the EDL, which was formed at the interface of electrode/electrolyte. The specific capacitance of different carbon derivative electrodes are presented in the Fig. 4d.[S6-S19]

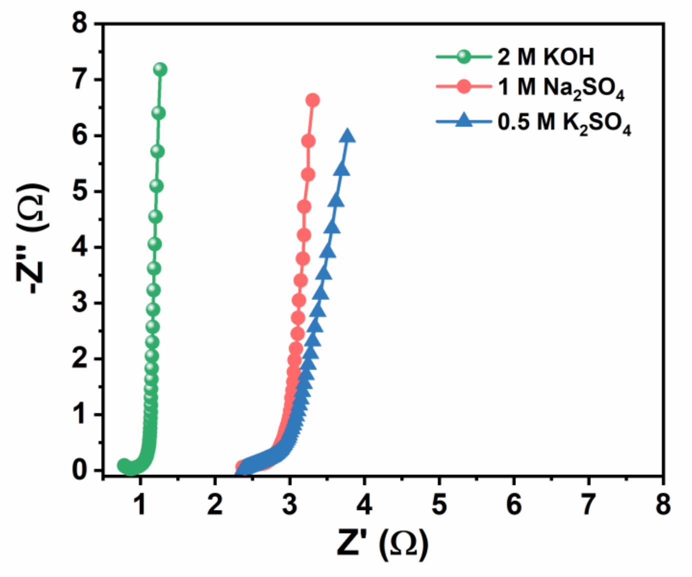

Fig. S3 (a) EIS spectraof SHAC2 electrode in different electrolytes.

Note 3

Molecular dynamics simulations

Fig. S4 shows a schematic of the side view of the supercapacitor system. Fig 3e of the main text corresponds to the region enclosed by the black dashed lines in Fig. S4. Each pore wall was made of a square lattice of Lennard-Jones (LJ) particles with spacing of 0.17 nm. To model the electrolytes used in the experiments, we took the force field parameters from the references [S20] and [S21] for KOH and Na_2SO_4, respectively. We note that the Na_2SO_4 force field uses a scaled charge model while the charge is unscaled in the KOH model. To match with the forcefields of the electrolytes, two types of solvents model, TIP3P[S22] and TIP4P/2005[S23], were used for KOH and Na_2SO_4, respectively.

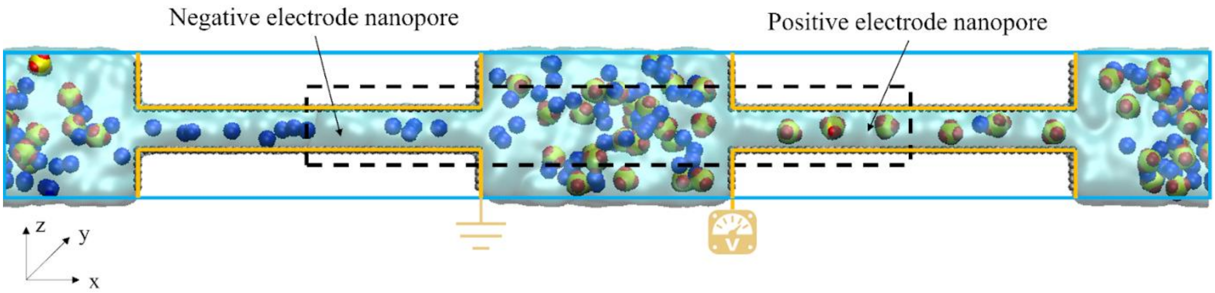

Fig. S4 Snapshot of the side view of the MD system (Na_2SO_4 electrolyte). The blue line denotes the simulation box. The yellow line denotes the position of the image plane. The dimension of the simulation box in x, y, and z directions are 28.2 nm, 2.6 nm, and 3.1 nm, respectively.

The LJ potential describing the non-electrostatic interactions, which is (r)=4(/r)12-(/r)6. The wall atoms were treated as carbons with the LJ parameters = 0.337 nm and = 0.23 kJ/mol. Under such interaction parameters, the nanopores considered in the main text were wetted by water without applied voltage, while only a small amount of ions was in the nanopores (i.e., such nanopores are ionophobic), as shown in Fig. S5, demonstrating the evolution of cation and anion densities during charging.

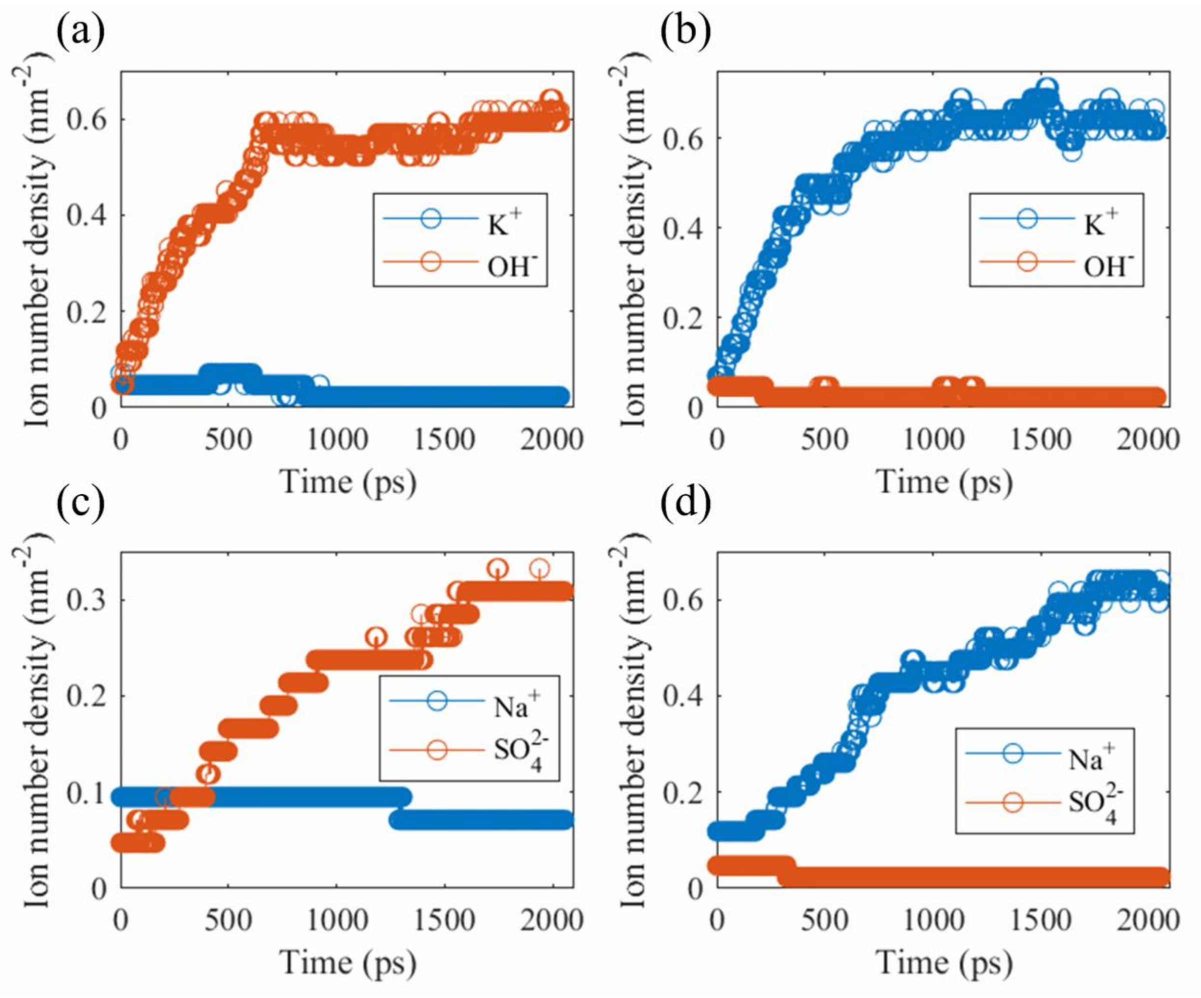

Fig. S5 Evolution of cation and anion densities for KOH and Na_2SO_4 electrolytes inside the positive (a, c) and negative (b, d) electrode nanopores during charging.

In all simulations, 2 fs time step and 1 ps time constant for the Nose-Hoover thermostat was used to control the temperature of electrolyte. The non-electrostatic interactions were computed with a cut-off distance of 1.2 nm and the neighbor list was updated every 10 steps. To take into account the electrostatic potential by the polorizable walls, the electrostatic interactions were computed by the PME method with solving an auxiliary Laplace equation.[S24] In the PME part, we used a real space cutoff of 1.2 nm and the FFT grid spacing of 0.1 nm. The auxiliary Laplace equation was discretized using the compact four-order stencil on the same grid with the FFT grid and solved each simulation step using the method of Green's function.

Notes on Video clips

Fig. 3f-g in the main text shows the quantitative charging of nanopores filled with two electrolytes, KOH and Na_2SO_4. Here we visualize the charging of KOH (Movie # video file 1) and Na_2SO_4 (Movie # video file 2) in the nanopores. For clarity, the water is not shown. The upper part of the videos shows the top view of the ions' trajectory (corresponds to Fig. 3e of the main text) during charging. The lower part of the videos shows the evolution of ions in positive and negative electrode pores, as well as the evolution of total net charges.

Note 4a

To check the influence of hierarchical pore ratios on energy-storage properties, several electrochemical characterizations including CV and GCD along with EIS (only in KOH electrolyte) were executed in three-electrode system (Fig. S6a–c) for SHAC and CAC electrodes at 50 mV/s scan rate, 5 A/g current density, and 5 mV alternating current (AC) amplitude in 2 M KOH, 1 M Na_2SO_4 and 0.5 M K_2SO_4 electrolytes. Clearly, in KOH electrolyte, the areas under the SHAC (except SHAC0.5) electrodes CV curves (Fig. S6a) are larger than those under CAC electrode CV curve. The SHAC (except SHAC0.5) electrodes also exemplified the longer charging and discharging curves, which indicate excellent electrochemical properties via specific capacitances that are 1.34 (SHAC0.5), 1.34(SHAC1), 2.84 (SHAC2), 1.78 (SHAC3), and 1.611 (SHAC4) (note that the IR drop is very high for SHAC0.5 and SHAC1 electrodes) folds higher than that of the CAC electrode (Fig. S6b). This occurs due to the greater surface areas of the SHAC electrodes. Among the SHAC electrodes, SHAC2 exhibits a better specific capacitance of 2.1, 1.6, 1.6, and 1.8 folds in KOH electrolyte, 1.2, 1.1, 1.0 and 1.1 folds in Na_2SO_4 electroltye, and 1.2, 1.1, 1.02, and 1.1 folds in K_2SO_4 electrolyte than SHAC0.5, SHAC1, SHAC3 and SHAC4, respectively. It also offers a reduced charge transfer resistance (Rct) (0.15 Ω) than SHAC3 (0.19 Ω) and SHAC4 (0.35 Ω) in all electrolytes (here only presented in KOH electrolyte).

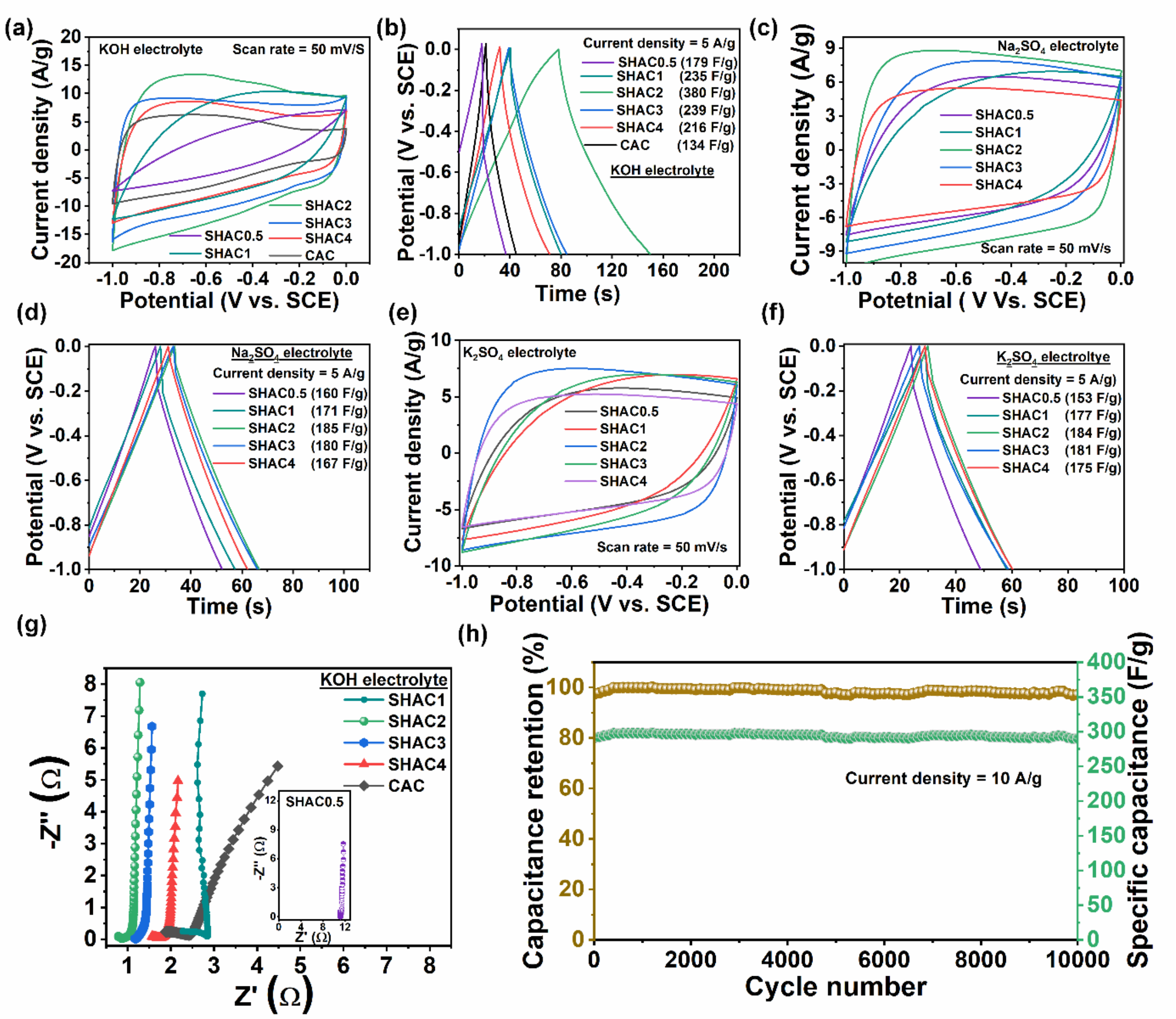

Fig. S6 Electrochemical properties of SHAC electrodes in KOH electrolyte [(a) CV, (b) GCD], Na_2SO_4 electrolyte [(c) CV and (d) GCD)] and K_2SO_4 electrolyte [(e) CV and (f) GCD]. (g) EIS curves as a function of the KOH activation concentration and compared with CAC electrodes. (h) GCD cycling stability of SHAC2 electrode in KOH electrolyte at the current density of 10 A/g.

Note 4b

Electrochemical reversibility of SHAC2 electrode in KOH electrolyte

To evaluate the electrochemical reversibility and rate capability of the optimized SHAC2 electrode, scan rate reliant CV and current density reliant GCD investigations were executed in KOH (2 M) electrolyte and acquired results are plotted in Fig. S7a and Fig. S7b. The CV curves

(Fig. S7a) have similar shapes at low and high scan rates without any distortion and the integral area under the CV curve enhances with the increase of scan rate, suggests that the SHAC2 electrode has better electrochemical reversibility. Likewise, except 1 and 2 A/g current density, all the GCD (Fig. S7b) curves have nearly triangular shapes without any potential drop even at elevated current densities. This signifies that the SHAC2 sample has high electrical conductivity. Distorted shape of GCD curves when applying 1 and 2 A/g current densities suggests that the active role of micropores in achieving excellent specific capacitance. Quantitative analysis of the discharge times from the GCD curves indicates superior specific capacitances (Fig. S7c) of 592 F/g (volumetric capacitance (C_v)=296 F/cm^3) at 1 A/g and 299 F/g (C_v = 150 F/cm^3) at 10 A/g with 50.5% rate capability.

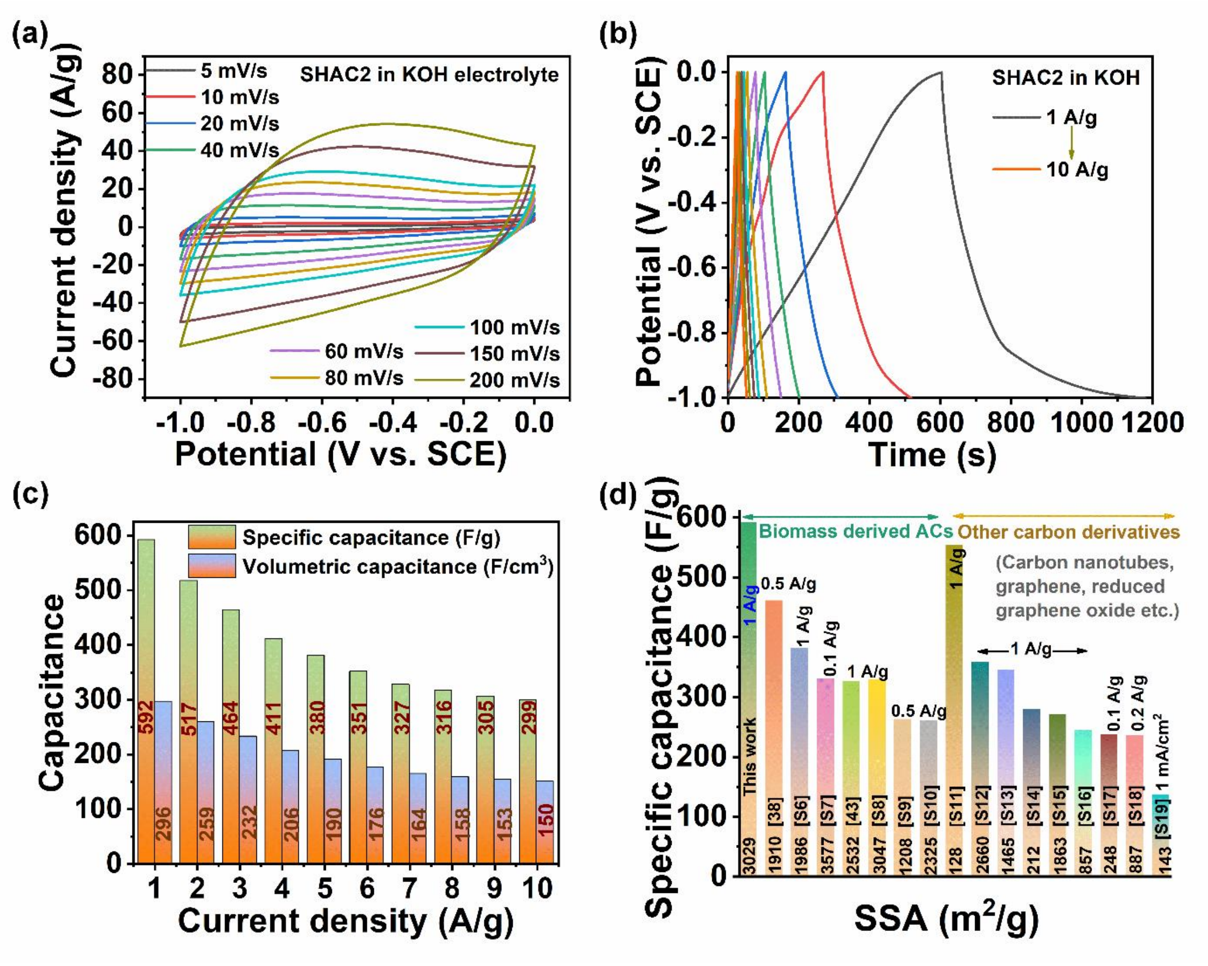

Fig. S7 Electrochemical properties of SHAC2 electrodes in KOH electrolyte: (a) scan rate reliant CV curves, (b and c) current density reliant GCD curves and corresponding specific/volumetric capacitances of SHAC2, respectively. (d) Specific capacitance comparison with biomass derived ACs and other carbon derivatives (references are displayed in square brackets)

As discussed above, micropores play a key role in obtaining the enhanced specific capacitances. Thus, in the general paradigm, the electrolyte can diffuse in both micro (if the micropores are suitable for ion adsorption) and mesopores when charging at a low current density but can access only key mesopores when charging at a high current density. Here, the SHAC2 electrode contains 66% micropores, thus, at higher current densities, its rate capability is 51.8% of that available at 2 A/g. However, it unveils a healthier specific capacitance of 268 F/g at 10 A/g, which is similar to or better than the results previously reported for biomass-derived ACs at 0.5 A/g or 1 A/g current densities. For instance, Liu et al.[S25] reported a jujun grass-derived hydrothermally carbonized AC, where the AC electrode delivers 220 F/g maximum specific capacitance when applying 1 A/g current density in a 6 M KOH electrolyte. For wood sawdust, Huang et al.[S26] established a possible specific capacitance by applying 0.5 A/g current density is about 225 F/g. Therefore, it is inferred that a well-balanced micro-to-mesopore ratio is crucial and is the reason that SHAC2 exhibits such an exceptionally high specific capacitance even in low concentration (2 M KOH) electrolyte. When applying 10 A/g current density, the GCD cycling (after functioning 10,000 cycles) stability of SHAC2 electrode (Fig. S6d) exhibits 97.15% retention of specific capacitance. Fig. S7d shows the comparison graph of the SHAC2 delivered specific capacitance with the specific capacitances of other biomass derived ACs and carbon derivatives like carbon nanotubes, graphene and reduced graphene oxides.

Note 5

To investigate the widening of potential window, the two electrode system based LSV curves of stainless steel electrodes were measured in both KOH (Fig. S8a) and hybrid electrolytes (Fig. S8b). As compared to KOH electrolyte, the hybrid electrolyte exhibited the over potential of OER at high voltage region and showed the possible driving voltage of 3.05 V, however, the voltage window may change depending on the chosen electrode. In addition, it appears that appropriate addition of the redox agent $K_3Fe(CN)_6$ is essential to enhance the SHAC2 electrode specific capacitance. The appropriate amount of redox agent serves to balance the EDLC and faradaic reactions via an auxiliary contribution of the redox $[[Fe(CN)_6]^{3-}/[Fe(CN)_6]^{4-}]$ couple during the energy storage process. The following redox reaction occurs via direct electron transfer[S27]:

$$[\mathrm{Fe(CN)}_6]^{3-} + \mathrm{e}^- \rightleftharpoons [\mathrm{Fe(CN)}_6]^{4-} \qquad (4)$$

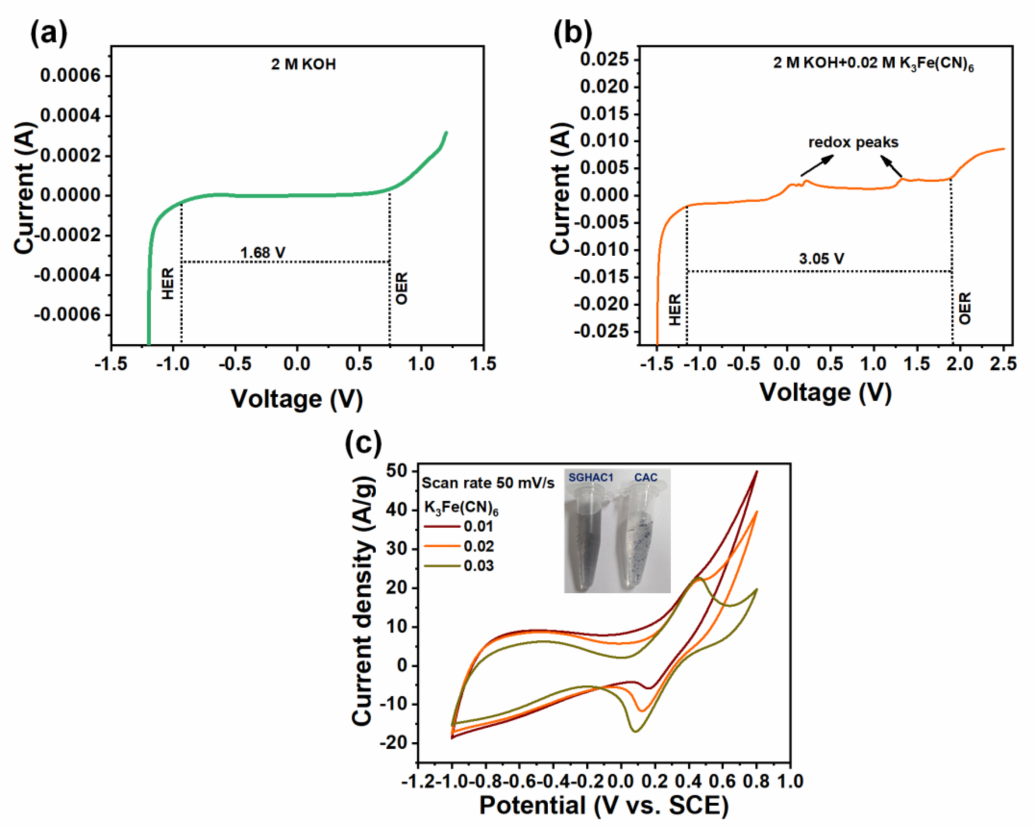

Fig. S8 LSV curves of the (a) KOH and (b) hybrid electrolytes. (c) CV curves of the SHAC2 electrodes at different $K_3Fe(CN)_6$ concentrations in KOH electrolyte (inset shows the digital photographs of SHAC2 and CAC samples after dispersion in the DI water).

CV measurements (potential window between -1 and 0.8 V) with different $K_3Fe(CN)_6$ concentrations (0.01, 0.02 and 0.03 M) in the 2 M KOH electrolyte are addressed Fig. S8c. The obtained results are presented in Fig. S8c. As seen in the Fig. S8c, at 0.01 M $K_3Fe(CN)_6$ concentration, weak contribution of redox peaks was observed due to an in sufficient redox-active species in hybrid electrolyte. When the concentration of $K_3Fe(CN)_6$ increased to 0.02 M in the 2 M KOH electrolyte, a pair of well-established redox peaks at 0.4 and 0.08 V along with quasi-rectangular capacitive curve in the –ve potential window were emerged in the CV curve. The presence of redox peaks confirms the battery type behaviour with faradic reactions on the carbon surface and the EDLC area is almost similar to the SHAC2 electrode measured in 0.01 M $K_3Fe(CN)_6$ concentration contained hybrid electrolyte. The $K_3Fe(CN)_6$ concentration further increases to 0.03 M in the hybrid electrolyte, the area under CV curve, particularly in the –ve potential window, decreases as compared to 0.02 M due to the dominant faradic reactions on the carbon surface.

Note 6

The effect of the mass of $K_3Fe(CN)_6$ cannot be ignored. Thus, we performed areal capacitance calculations for the SHAC2 electrode at 6 mA/cm^2 (= 5 A/g under these research conditions) in both KOH (394 mF/cm^2) and hybrid electrolytes (1270 mF/cm^2) and compared this difference with the specific capacitance difference. The areal capacitance is enhanced by approximately 3.24-fold in the hybrid electrolyte, indicates that effect of the mass of $K_3Fe(CN)_6$ on the specific capacitance calculation is negligible because the molar concentration of the KOH electrolyte is 100 times higher than the auxiliary electrolyte. Thus, the mass of the auxiliary electrolyte does not have a considerable effect on the specific capacitance calculation and need not be considered. The unique pore structure, high SSA, wettability and the availability of reasonable amount of surface oxygen functional groups are the main sources in the enhanced electrochemical activity of SHAC2. The same quantities of SHAC2 and CAC powder samples were dispersed in de-ionised water under identical conditions to observe the hydrophilic nature of the samples. The result was photographed and is shown in the inset of Fig. S8c. SHAC2 exhibits high water dispersion. This indicates that the better hydrophilic nature of the SHAC2 electrode, which is also responsible for producing its unequalled specific capacitance. Thus, further electrochemical measurements were performed in the hybrid electrolyte with 0.02 M of $K_3Fe(CN)_6$ as a redox additive.

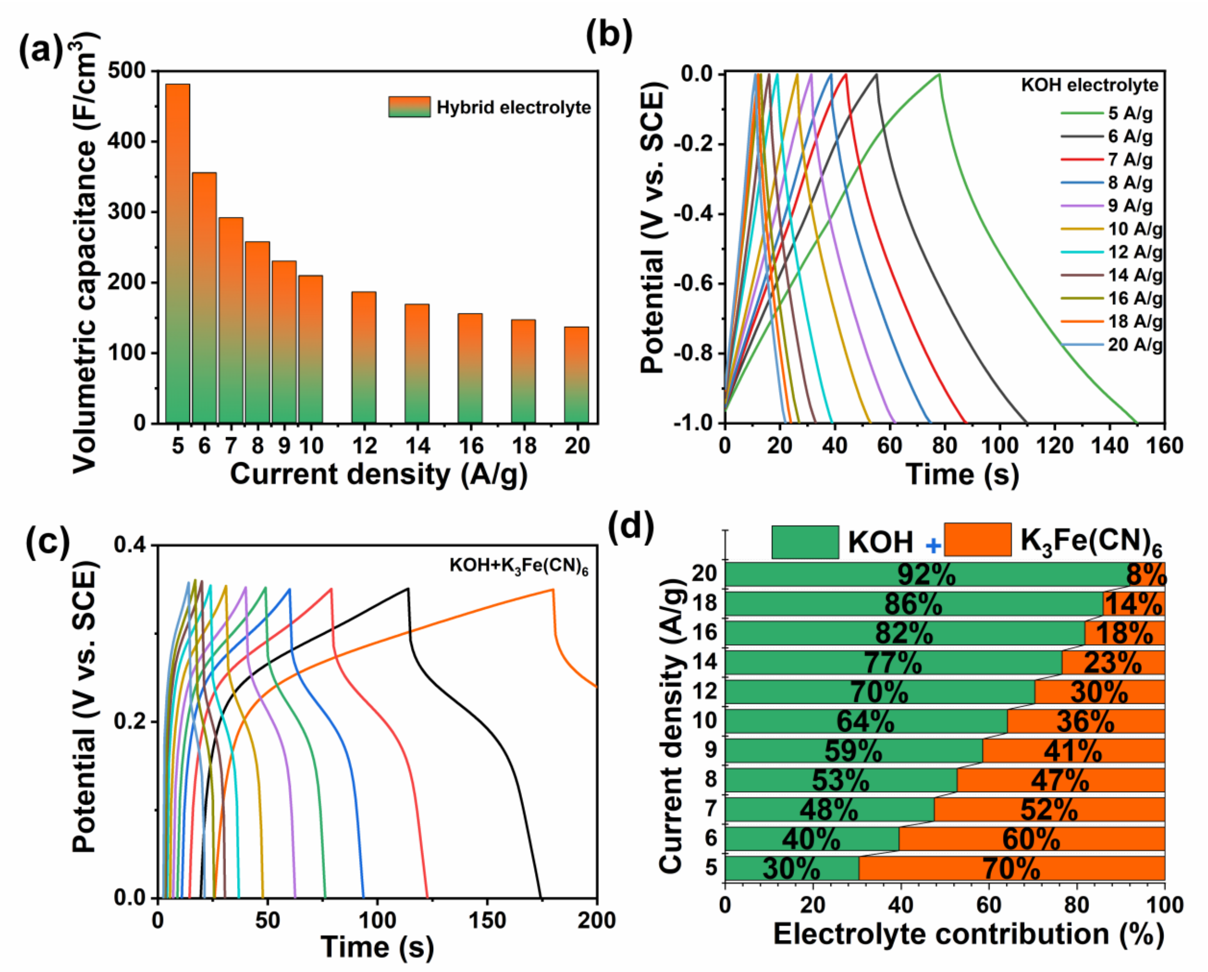

Fig. S9 (a) Volumetric capacitance of SHAC2 electrode in hybrid electrolyte. GCD curves of SHAC2 electrode as a function of current density (5-20 A/g) (b) in KOH electrolyte and (c) in hybrid electrolyte (Fig. b shows the magnified GCD curves for intending to discuss the pattern conversion from non-triangular shape to triangular shape with increasing the current density). (d) Redox species contribution in obtaining the specific capacitance

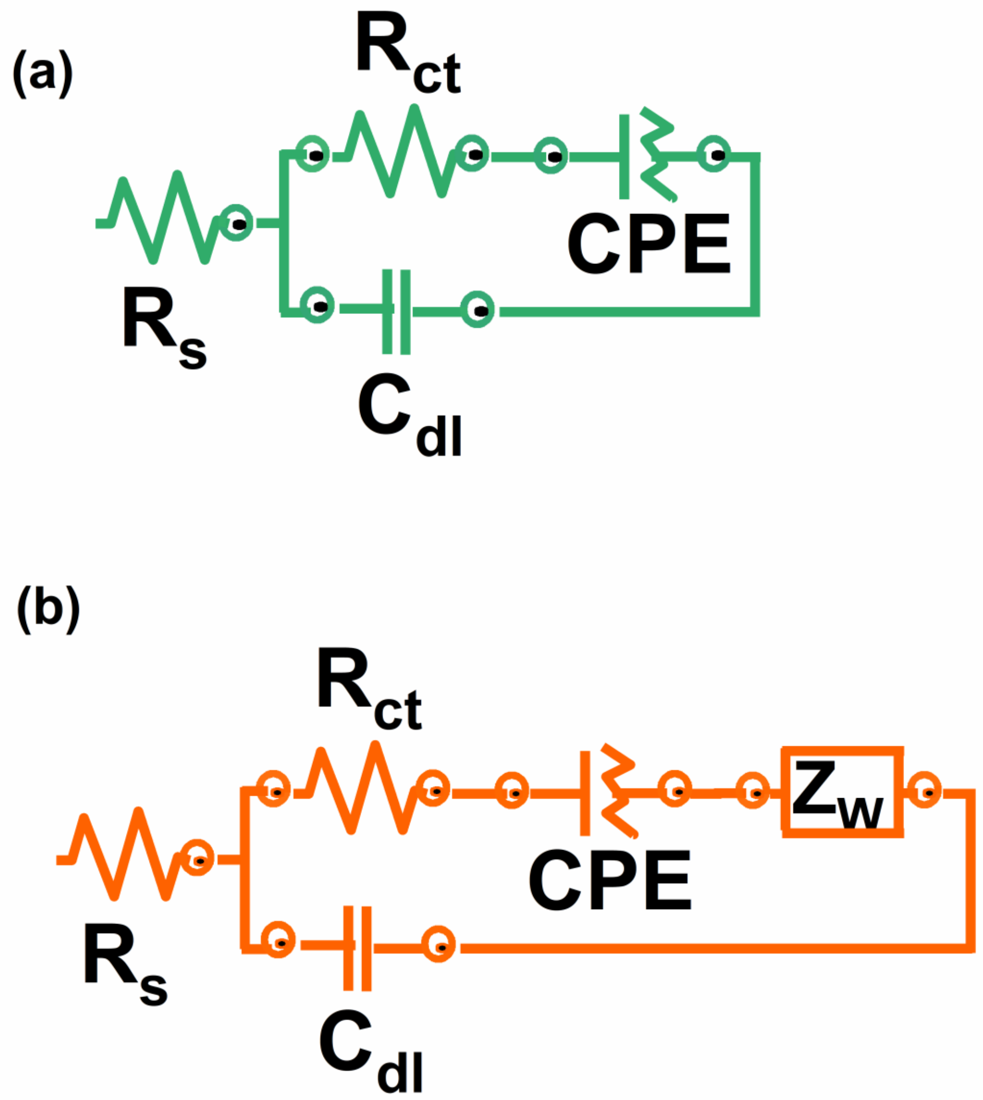

Fig. S10 Electrochemical circuit fitting of SHAC2 electrode when measured in (a) KOH and (b) hybrid electrolytes

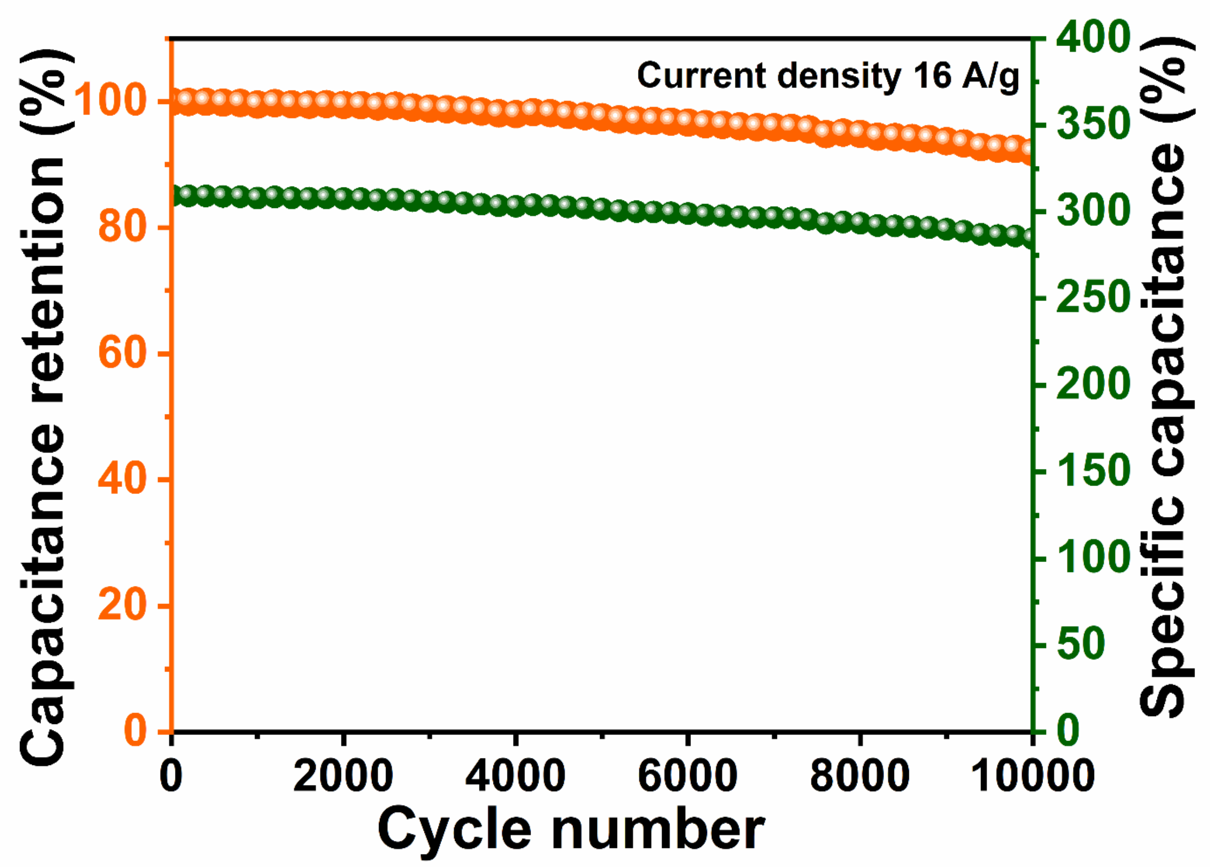

Fig. S11 GCD Cycling stability with capacitance retention percentage and specific capacitance values of SHAC2 electrode in hybrid electrolyte.

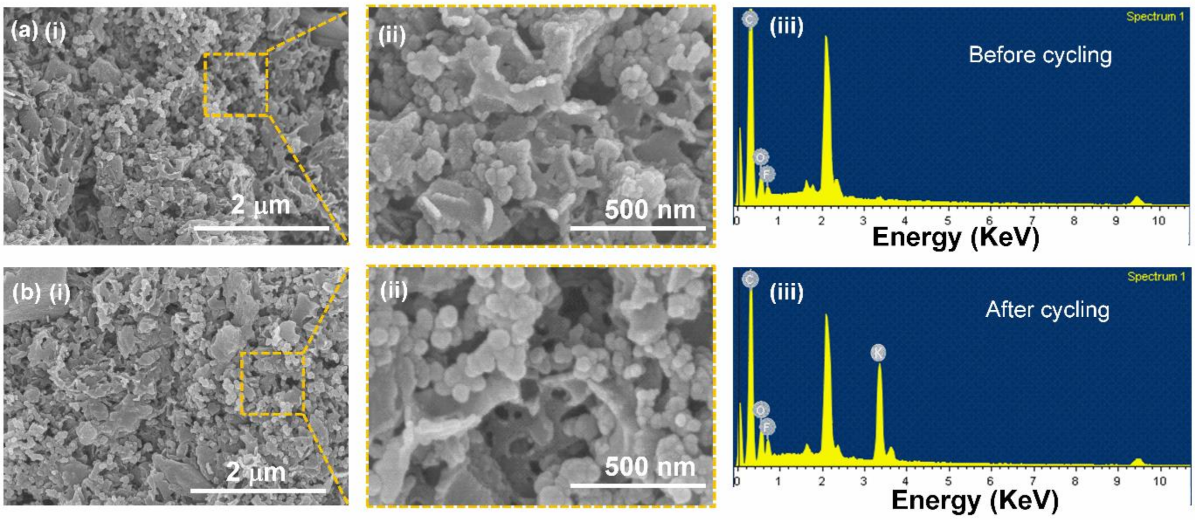

Fig. S12 (a) Before and (b) after cycling FESEM images and EDAX spectra of SHAC2 electrodes in hybrid electrolyte.

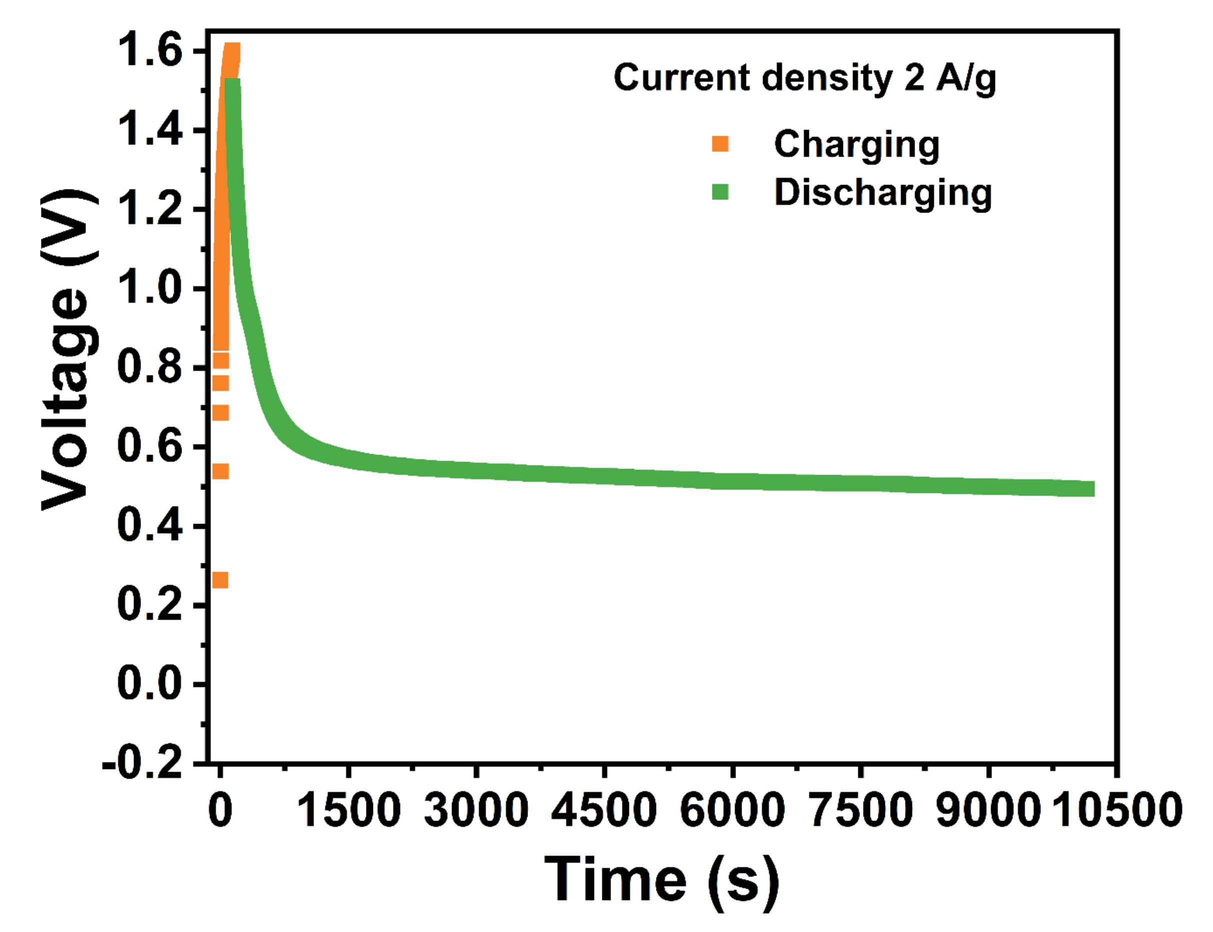

Fig. S13 Self-discharging GCD curves of the SHAC2-based fabricated PCSSC.

Table S1: Energy and power density comparisons between our work and previous reports

Source	Device type	Electrolyte	Voltage window (V)	Energy density (Wh/kg)	Power density (W/Kg)	Reference
Silver grass-derived AC	Symmetric	2M KOH+ 0.02M $K_3Fe(CN)_6$	0–1.6	34	750	This work
Baobab fruit shell-derived AC	Symmetric	PVA-4MKOH	0–1.8	21	400	[61]
Algae-derived AC	Symmetric	2M KOH	0–1	20	332	[62]
Jute fiber-derived AC	Symmetric	1M Na_2SO_4	0–1.6	15.44	402.78	[63]
Pumpkin-derived AC	Symmetric	1M Na_2SO_4	0–1.6	22.1	450	[64]
lotus seedpods-derived AC	Symmetric	6M KOH	0–1	12.5	260	[65]
$NiMoO_4$//AC	Hybrid	1MKOH	0–1.6	32	787	[2]
Ni_3Se_2 NSs@CF//AC	Hybrid	1MKOH	0–1.6	33	667	[66]
2D Co_9S_8 nanoflake//AC	Hybrid	30 wt% KOH	0–1.6	31.4	200	[67]
MoS_2/NiS//AC	Hybrid	1M KOH	0–1.48	31	155.4	[68]
CoM NS@CoP//AC	Hybrid	1M KOH	0–1.5	27.6	217.3	[69]
Ti_3C_2Tx// PANI@rGO	Assymmetric	3M H_2SO_4	0–1.5	17	220	[70]

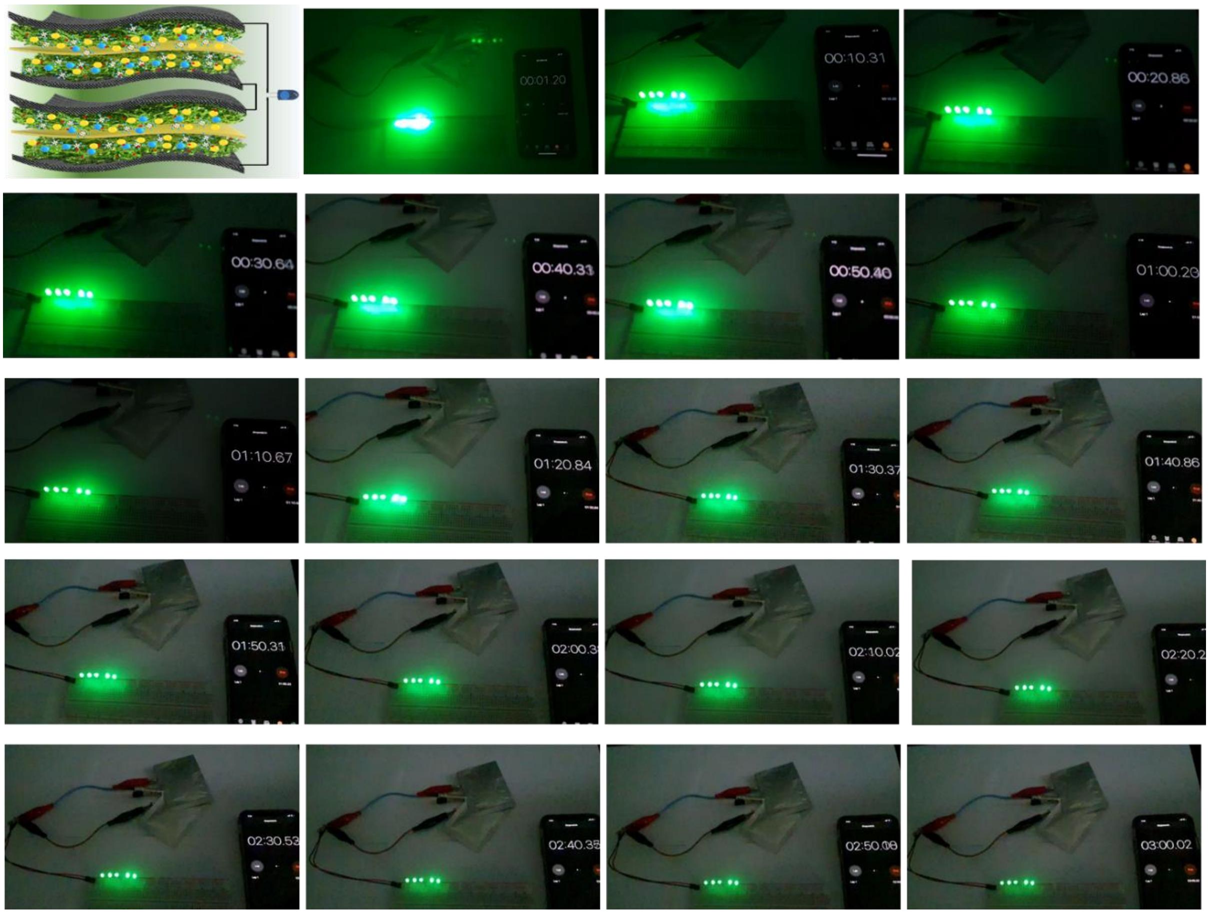

Fig. S14 operational stability of SDPC supercapacitors when driving the green color LEDs and observed that the LEDs continues to glow even after three minutes, indicating their possible utilization in the real-world application with the outstanding performance.

References

S1 S. Chen, Y. Cao, and J. Feng, *ACS Appl. Mater. Interfaces*, 2014, **6**, 349-356.

S2 Y. Zhu, S.Murali, M. D. Stoller, K. J. Ganesh, W. Cai, , P. J. Ferreira, A. Pirkle, R. M.Wallace, K. A. Cychosz, M. Thommes, D. Su, E. A. Stach, R. S. Ruoff, *Science,* 2011, **332**, 1537-1541.

S3 R. Chen, L. Li, Z. Liu, M. Lu, C. Wang, H. Li, W. Ma, S. Wang, *J. Air Waste Manage. Assoc.*, 2017, **67**, 713-724.

S4 S. Sedghi, S. H. Madani, C. Hu, A. Silvestre-Albero,W. Skinner, P. Kwong, P. Pendleton, R. J. Smernik, F. Rodríguez-Reinoso, M. J. Biggs, *Carbon*, 2015, **95**, 144-149.

S5 P. M. Blass, X. L.Zhou, J. M. White, J. Phys. Chem., 1990, **94**, 3054-3062.

S6 J. Wang, F. Qin, Z. Guo and W. Shen, *ACS Sustainable Chem. Eng.*, 2019, **7**, 11550-11563.

S7 T. Shang, Y. Xu, P. Li, J. Han, Z. Wu, Y. Tao and Q.-H, *Nano Energy*, 2020, **70**, 104531.

S8 C. Shi, L. Hu, K. Guo, H. Li, T. Zhai, Adv. *Sustainable Syst.*, 2017, **1,** 1600011

S9 T. Ouyang, K. Cheng, F. Yang, L. Zhou, K. Zhu, K. Ye, G. Wang and D. Cao, *J. Mater. Chem. A*, 2017**,** **5**, 14551-14561.

S10 C. Li, W. Wu, P. Wang, W. Zhou, J. Wang, Y. Chen, L. Fu, Y. Zhu, Y. Wu, W. Huang, *Adv. Sci.*, 2019, **6**, 1801665.

S11 W. Chen, R. B. Rakhi and H. N. Alshareef, *Nanoscale*, 2013, **5**, 4134-4138.

S12 Z. Song, D. Zhu, L. Li, T. Chen, H. Duan, Z. Wang, Y. Lv, W. Xiong, M. Liu and L. Gan, *J. Mater. Chem. A*, 2019, **7**, 1177-1186.

S13 Y. Chen, Y. Li, F. Yao, C. Peng, C. Cao, Y. Feng and W. Feng, *Sustainable Energy Fuels*, 2019, **3**, 2237-2245.

S14 B. Gao, C. Hu, H. Fu, Y. Sun, K. Li and L. Hu, *Electrochim. Acta*, 2020, **361**, 137053.

S15 Y. Zhou, P. Jin, Y. Zhou and Y. Zhu, *Sci. Rep.*, 2018, **8**, 9005.

S16 X. Fu, A. Chen, Y. Yu, S. Hou and L. Liu, *Chemistry – An Asian J.*, 2019, **14**, 634-639.

S17 X. Peng, H. Cao, Z. Qin, C. Zheng, M. Zhao, P. Liu, B. Xu, X. Zhou, Z. Liu and J. Guo, *Electrochim. Acta*, 2019, **305**, 56-63.

S18 Z. Huang, H. Guo and C. Zhang, *Compos. Commun.*, 2019, **12**, 117-122.

S19 C. Guo, Y. Zhang, T. Zeng, D. Huang, Q. Wan and N. Yang, *Carbon*, 2020, **157**, 298-307.

S20 A. Godec, M. Gaberšček, J. Jamnik, D. Janežič, F. Merzel, *Phys. Chem. Chem. Phys.*, 2010, **12**, 13566-13573.

S21 I.M. Zeron, J.L.F. Abascal, C. Vega, *J. Chem. Phys.*, 2019, **151**, 134504.

S22 W.L. Jorgensen, J. Chandrasekhar, J.D. Madura, R.W. Impey, M.L. Klein, *J. Chem. Phys.*, 1983, **79**, 926-935.

S23 J.L.F. Abascal, C. Vega, *J. Chem. Phys.*, 2005, **123**, 234505.

S24 A.V. Raghunathan, N.R. Aluru, Phys. Rev. E, 2007, **76**, 011202.

S25 Y. Liu, B. Huang, X. Lin, Z. Xie, *J. Mater. Chem. A*, 2017, **5**, 13009-13018.

S26 H. Huang, J. Cui, G. Liu, R. Bi and L. Zhang, *ACS Nano*, 2019, **13**, 3448-3456.

S27 V. Horvat-Radošević, K. Kvastek, D. Križekar, *Croat. Chem. Acta*, 1997, **70**, 537-561.